Int J Adv Manuf Technol (2014) 74:319–334
DOI 10.1007/s00170-014-5967-4

ORIGINAL ARTICLE

Numerical analysis of heat generation and temperature field in reverse dual-rotation friction stir welding

L. Shi · C. S. Wu · H. J. Liu

Received: 21 February 2014 / Accepted: 18 May 2014 / Published online: 1 June 2014

Abstract A 3D model is developed for numerical analysis for heat generation, temperature field, and material flow in reverse dual-rotation friction stir welding (RDR-FSW) process. The reverse rotation of the assisted shoulder and the tool pin is considered to determine the heat generation rate. Friction heat, plastic deformation heat, and their partition coefficients are analyzed. Due to the tool pin and assisted shoulder being separated and reversely rotated independently, the temperature difference between the advancing and retreating sides is weakened. The reverse material flow is beneficial to the uniformity of both the temperature and microstructure at the advancing and retreating sides. The calculated temperature profiles agree well with the corresponding experimentally measured values.

Keywords Heat generation · Temperature field · Reverse dual-rotation friction stir welding · Numerical analysis

1 Introduction

Friction stir welding (FSW) is a solid-state joining process which is energy efficient, environment friendly, and versatile [1–3]. It has been widely used to weld almost all series of aluminum alloy because of its advantages of lower residual stress and distortion, and it is almost defect free in comparison with fusion-based welding process. This process is being widely applied in industries such as automotive, aerospace, ship building, and high-speed trains [4].

In conventional FSW, a nonconsumable rotating tool with a specially designed pin and shoulder is inserted into the abutting edges of the plates to be joined and traverses along the line of the joint [1, 2]. During the process, the tool makes firm contact with the workpiece, and heat is generated by friction and plastic deformation at the tool-workpiece contact interfaces softening the material being welded. Severe heat generation and plastic material flow of this plasticized metal occurs as the tool is rotating and traversing along the welding direction [2]. Plastic material is transported from the front of the tool to the trailing edge to form a joint behind the tool [2]. Due to the rotation and motion of the tool, some differences of heat transfer and material flow behavior occur between the advancing side (AS) and the retreating side (RS), leading to corresponding differences of the microstructures and mechanical properties at both sides, which has a negative influence on the performance of the welded structure [5, 6]. During conventional FSW, in order to generate enough energy for the process, large welding torque and plunge force are needed, so the welding equipment is large in volume, and complex clamping equipment are necessary. Usually, the shoulder diameter is threefold to the plate thickness from the view of the weld formations and mechanical properties in the conventional FSW. The highest velocity at the outer edge of the shoulder may lead to overheating or even incipient melting that occurs along the shoulder edge of the weld surface, which depends on the materials to be welded and the applied process conditions [7, 8]. These phenomena are particularly severe during welding thick plate since larger shoulder diameter should be utilized with the increase of plate thickness. To solve the abovementioned problems, the dual-rotation FSW has been proposed at TWI as a variant technique [8]; Liu et al. made further improvements of this novel FSW technology subsequently [7, 9]. The key feature is that the tool pin and assisted

L. Shi · C. S. Wu (✉)
MOE Key Lab for Liquid-Solid Structure Evolution and Materials Processing, Institute of Materials Joining, Shandong University, Jinan 250061, China
e-mail: wucs@sdu.edu.cn

H. J. Liu
State Key Laboratory of Advanced Welding and Joining, Harbin Institute of Technology, Harbin 150001, China

shoulder are separately designed and manufactured; in this way, the tool pin and assisted shoulder can rotate independently [7, 9] allowing for a relatively high-rotating speed of the tool pin without a corresponding increase in the rotating speed of the assisted shoulder. Thus, the tendency towards overheating or incipient melting can be reduced through optimizing rotation speeds of both the tool pin and the assisted shoulder. Because of the different rotating direction of the tool pin and the assisted shoulder, the differences between AS and RS are reduced and the mechanical property of the weld joint can be improved. Due to the opposite rotating direction of the tool pin and the assisted shoulder, the welding torque exerted on the workpiece by the reverse rotating assisted shoulder is in the reverse direction to that of the rotating tool pin, thus the total welding torque exerted on the workpiece by the RDR-FSW tool system is reduced, so the clamping equipment can be simplified. When the process load and clamping requirement are reduced, the size and mass of the FSW equipment and the fixture can be lowered [7, 9].

In conventional FSW process, the heat transfer and material flow are complex because of the variety of the base material properties, the welding parameters, and the tool geometry. However, since the tool pin and assisted shoulder are separated and reverse rotating independently in RDR-FSW, the number of the process parameters and the complexity of the underlying physical mechanisms increase, which makes the process more complex. The complicated interactions among the various physical variables and welding parameters simultaneously affect the heat transfer and material flow during the RDR-FSW process and determine the final microstructure and properties of the welded joints. In order to optimize the process and the relevant microstructure and mechanical properties of the joints, a fundamental knowledge of the complex process during the RDR-FSW should be required, and the rigorous numerical model coupled with experimental results is very suitable. However, at present, no detailed researches on the RDR-FSW have been carried out except for a few papers that demonstrated the advantages of this novel FSW through experiments [7–9]. There is no appropriate investigation on the mechanism of the RDR-FSW process until now. As a novel FSW, RDR-FSW is the modification of the conventional FSW, and it has some similarities to the conventional FSW in aspects of numerical modeling. Although significant progress in the quantitative understanding of the conventional FSW process has been made [10–20], no detailed researches on numerical modeling of reverse dual-rotation friction stir welding has been studied. A rigorous numerical model is developed to quantitatively understand heat generation, material flow, and temperature profile in reverse dual-rotation friction stir welding in this paper. The reverse rotation of the assisted shoulder and the tool pin is considered to model the heat generation rate. Heat generated due to plastic deformation and friction at the tool-workpiece interfaces are described, and the viscous dissipation near the tool in the nugget zone and thermal mechanically affected zone (TMAZ) is also considered. Material flow during the RDR-FSW process has also been analyzed. The numerical simulation results lay the foundation for establishing the knowledge base and optimizing the process.

2 Numerical modeling

Figure 1 shows the main difference between the RDR-FSW and the conventional FSW processes. As shown in Fig. 1a, the tool system in RDR-FSW can be divided into two main parts—the tool pin with the subsize concave shoulder and the assisted shoulder. The tool pin is mounted on a subsize concave shoulder. Both the tool pin and subsize concave shoulder are machined on the shaft and fixed on the spindle of the FSW machine. In this way, the tool pin rotates with the spindle during the welding process with the same rotation speed and direction. During the welding process, the assisted shoulder rotates independently and reversely driven by two servo motors. Owing to the existence of the subsize concave shoulder, it is helpful to prevent the overflow of plasticized materials at the interface between the rotating tool pin and the reversely assisted shoulder. During the process of RDR-FSW, the rotation direction of the assisted shoulder is reverse to that of the rotating tool pin with the subsize concave shoulder, and there is a difference when the retreating side and the advancing side are defined when compared with the joints welded by conventional FSW. For RDR-FSW, the half plate where the tangential direction of the rotating tool pin with the subsize concave shoulder (not the assisted shoulder) is the same as the welding direction is called the advancing side, with the other side as the retreating side, as shown in Fig. 1.

Figure 2 demonstrates the difference in modeling the RDR-FSW and the conventional FSW process. The geometry model for the RDR-FSW is shown in Fig. 2a. A 3D Cartesian coordinate system is established on the plate. The origin of the coordinate is located at the bottom of the workpiece under the axis of the tool. The welding direction is identical to the positive x-axis; the thickness of the plate is given on the z-axis and the positive direction towards to the top of the workpiece. Figure 3 shows the top view of the mesh system in this simulation of the RDR-FSW process which has a total of 89,640 mesh elements. For simplification, the tilt angle and the thread of the tool pin are not considered. The geometrical feature of the RDR-FSW tool is not included in this geometric model but being treated as a rigid body. In order to compare heat generation and temperature distribution in RDR-FSW with conventional FSW, a conventional FSW model is also established at the same tool and workpiece dimension as well as the same welding parameters. Figure 2b depicts the geometric model of conventional FSW.

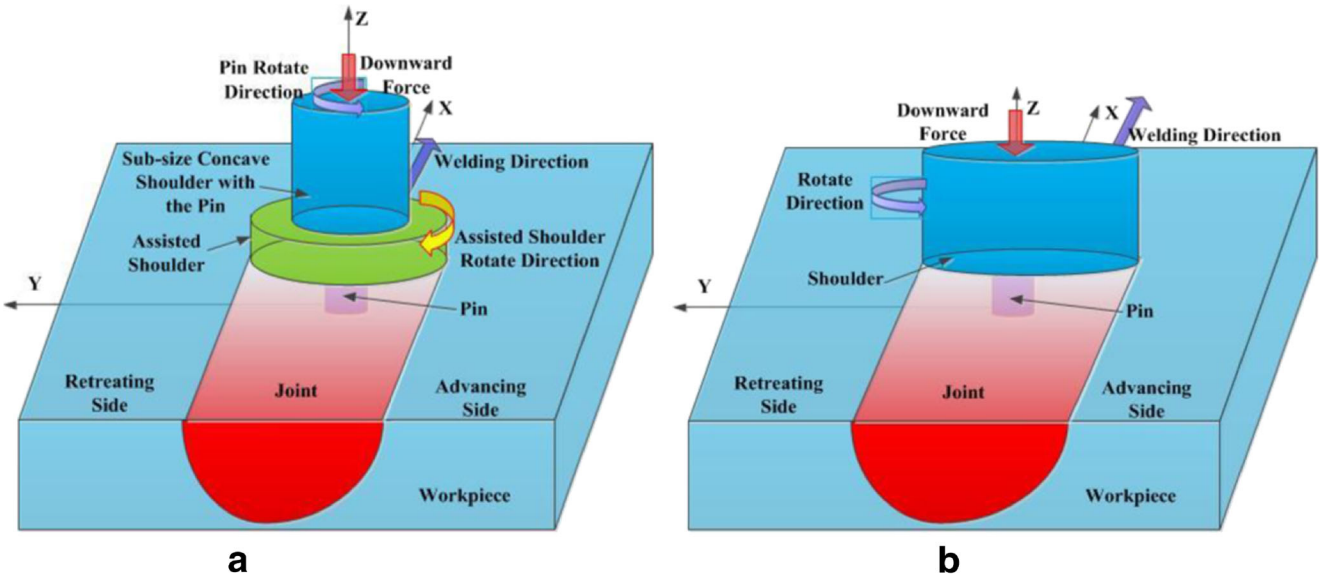

Fig. 1 Schematic drawings of **a** reverse dual-rotation friction stir welding (RDR-FSW) and **b** conventional FSW

Table 1 gives the dimension of the tool and workpiece in the simulation. The size of the assisted shoulder is 14 mm in the outer diameter and 10 mm for the inner diameter which is of the same size for the outer diameter of the subsize concave shoulder. The 0.1-mm gap between the assisted shoulder and the subsize concave shoulder is ignored. The size of the shoulder in conventional FSW is 14 mm in diameter. The tool pin has a length of 4.8 mm, a diameter of 5 mm at the root, and 4 mm at the tip both in RDR-FSW and conventional FSW. The test workpieces in the experiment are in dimensions of 300 mm×160 mm×5 mm. In order to save time for computations, the plates for the calculation are in dimensions of 100 mm×100 mm×5 mm.

2.1 Governing equations

Only the quasi-steady state is dealt with in this study. During the welding period, the material near the tool is heated to a relatively high temperature, and only the plastic deformation is considered. The material during the RDR-FSW process is assumed to behave as an incompressible and single-phase non-Newtonian flow. The density variation was ignored following Boussinesq's approximation.

The continuity equation is written as:

$$\frac{\partial u_i}{\partial x_i} = 0 \tag{1}$$

where u is the velocity of material flow, and index notation for $i=1$, 2, and 3 representing the x, y, and z directions, respectively.

The momentum equation:

$$\rho\frac{\partial u_i u_j}{\partial x_i} = -\frac{\partial p}{\partial x_j} + \frac{\partial}{\partial x_i}\left(\mu\frac{\partial u_j}{\partial x_i} + \mu\frac{\partial u_i}{\partial x_j}\right) - \rho U\frac{\partial u_j}{\partial x_j} \tag{2}$$

where ρ is the density, p is the pressure, U is the welding speed, and μ is the non-Newtonian viscosity.

The thermal energy conservation equation can be written as follows:

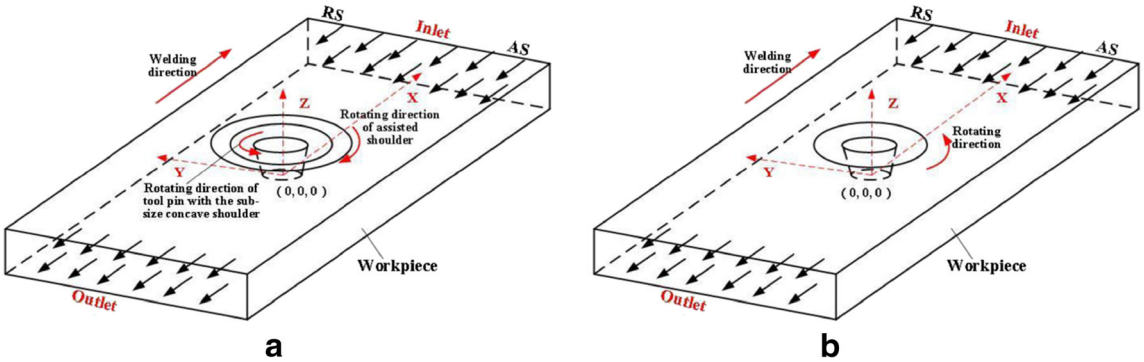

Fig. 2 Model in the simulation of **a** RDR-FSW and **b** conventional FSW process

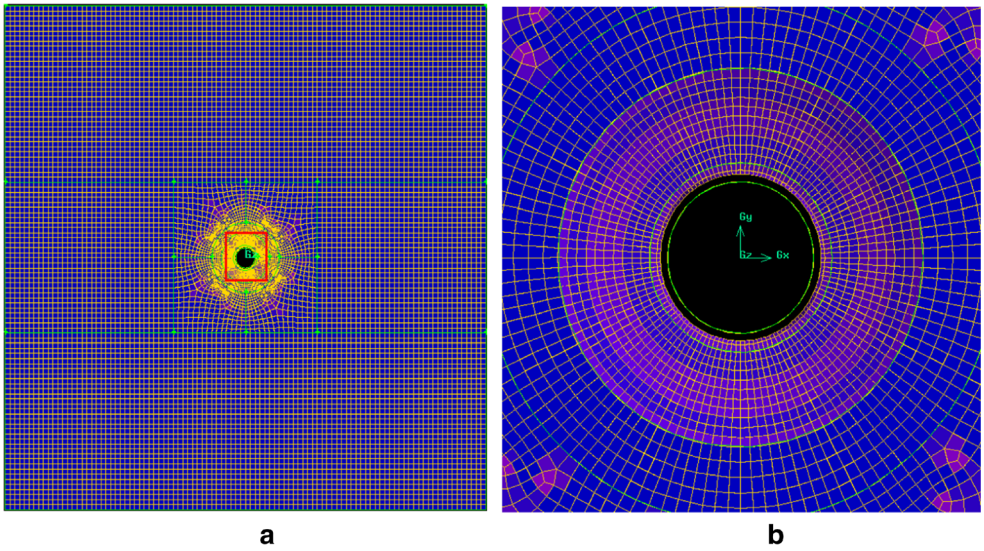

Fig. 3 Mesh system in the simulation of RDR-FSW **a** top views of the total workpiece and **b** local view of the mesh around the tool (enlarged of the red area in **a**)

$$\rho C_{\mathrm{p}} \frac{\partial (u_{\mathrm{i}} T)}{\partial x_{\mathrm{i}}} = -\rho C_{\mathrm{p}} U \frac{\partial T}{\partial x_1} + \frac{\partial}{\partial x_{\mathrm{i}}} \left(k \frac{\partial T}{\partial x_{\mathrm{i}}} \right) + S_{\mathrm{v}} \tag{3}$$

where k is the thermal conductivity, C_p is the specific heat of the material, T is the temperature, and the source term S_v represents the viscous dissipation source term due to plastic deformation near the tool in the nugget zone and TMAZ which can be calculated as [21]:

$$S_v = f_m \mu \Phi \tag{4}$$

where f_m is an arbitrary constant that indicates the extent of atomic mixing in the system, and Φ can be given by [21]:

$$\Phi = 2\left(\left(\frac{\partial u_1}{\partial x_1} \right)^2 + \left(\frac{\partial u_2}{\partial x_2} \right)^2 + \left(\frac{\partial u_3}{\partial x_3} \right)^2 \right) + \left(\frac{\partial u_1}{\partial x_2} + \frac{\partial u_2}{\partial x_1} \right)^2 + \left(\frac{\partial u_1}{\partial x_3} + \frac{\partial u_3}{\partial x_1} \right)^2 + \left(\frac{\partial u_3}{\partial x_2} + \frac{\partial u_2}{\partial x_3} \right)^2 \tag{5}$$

Because the material is being modeled with a CFD model, it is necessary to find a function to describe the viscosity of the material. The calculation of viscosity needs the local values for effective strain rate and temperature. Viscosity can be calculated as a function of flow stress and effective strain rate using Perzyna's viscoplasticity model [22]:

$$\mu = \frac{\sigma}{3\dot{\bar{\varepsilon}}} \tag{6}$$

where $\dot{\bar{\varepsilon}}$ is the effective strain rate and σ is the flow stress introduced by Sheppard and Wright for a high-strain rate and large bulk deformation processes of metals, and was given as [23, 24]:

$$\sigma = \frac{1}{\alpha} \ln \left\{ \left(\frac{Z\left(T, \dot{\bar{\varepsilon}}\right)}{A} \right)^{\frac{1}{n}} + \left[1 + \left(\frac{Z\left(T, \dot{\bar{\varepsilon}}\right)}{A} \right)^{\frac{2}{n}} \right]^{\frac{1}{2}} \right\} \tag{7}$$

where Z is the Zenner-Hollomon parameter which is given in the following equation [24]:

$$Z\left(T, \dot{\bar{\varepsilon}}\right) = \dot{\bar{\varepsilon}} \exp\left(\frac{Q}{RT} \right) = A[\sinh(\alpha\sigma)]^{\frac{1}{n}} \tag{8}$$

Table 1 Tool and workpiece dimensions for RDR-FSW and conventional FSW

Items	RDR-FSW	Conventional FSW
Shoulder diameter/mm	14.0 mm for assisted shoulder; 10.0 mm for subsize concave shoulder	14.0 mm
Pin diameter/mm	5.0 mm at the root; 4.0 mm at the tip	Same to RDR-FSW
Pin length/mm	4.8 mm	Same to RDR-FSW
Workpiece dimension	100 mm×100 mm×5 mm	Same to RDR-FSW

where T is the temperature, Q is the temperature-independent activation energy, R is the gas constant, α, and A and n are the material constants which can be obtained from open literature [25].

$\dot{\bar{\varepsilon}}$ is given as follows [16]:

$$\dot{\bar{\varepsilon}} = \sqrt{\frac{2}{3}\left[\sum_{i=1}^{3}\left(\frac{\partial u_i}{\partial x_i}\right)^2 + \frac{1}{2}\left(\frac{\partial u_1}{\partial x_2}+\frac{\partial u_2}{\partial x_1}\right)^2 + \frac{1}{2}\left(\frac{\partial u_1}{\partial x_3}+\frac{\partial u_3}{\partial x_1}\right)^2 + \frac{1}{2}\left(\frac{\partial u_3}{\partial x_2}+\frac{\partial u_2}{\partial x_3}\right)^2\right]} \tag{9}$$

From Eqs. 6, 7, and 8, the equation for calculating the non-Newtonian viscosity in this model can be written as follows:

$$\mu = \frac{1}{3\,\dot{\bar{\varepsilon}}^{\alpha}} \ln\left\{\left(\frac{Z\left(T,\dot{\bar{\varepsilon}}\right)}{A}\right)^{\frac{1}{n}} + \left[1+\left(\frac{Z\left(T,\dot{\bar{\varepsilon}}\right)}{A}\right)^{\frac{2}{n}}\right]^{\frac{1}{2}}\right\} \tag{10}$$

2.2 The boundary conditions

Previous work showed that in conventional FSW, heat is generated mainly near the interface between the tool and the workpiece [26]. Similar to conventional FSW process, during RDR-FSW process, heat is generated due to friction and plastic deformation at the tool-workpiece interfaces. Figure 4 shows schematically the contact interfaces between the tool-workpiece. The local interfacial heat generation due to friction is the product of the frictional force and the sliding velocity. The interfacial deformation heat is the product of shear stress and the velocity of the workpiece material which sticks to the tool as it moves [16]. During RDR-FSW process, ω_1 represents the rotating speed of the pin (also the subsize concave shoulder) in counterclockwise direction, while ω_2 represents the rotating speed of the assisted shoulder in clockwise direction as is shown in Fig. 4.

2.2.1 Heat flux boundary of the assisted shoulder

The plunge force is assumed to be applied to the tool contact interface uniformly. The frictional force on elemental area dA would be given as follows:

$$df = \mu_f P_2 d\mathrm{A} \tag{11}$$

where P_2 is the plunge force of assisted shoulder and μ_f is the friction coefficient at the tool-workpiece contact interface as a function of local temperature [27]. Temperature-dependent friction coefficient of the workpiece and the tool is shown in Fig. 5.

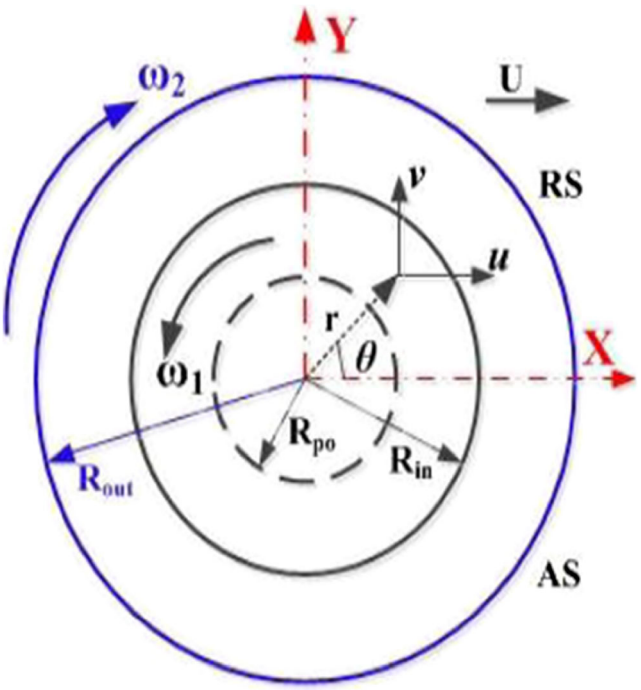

Fig. 4 A schematic illustration of tool-workpiece contact interfaces at tool shoulder

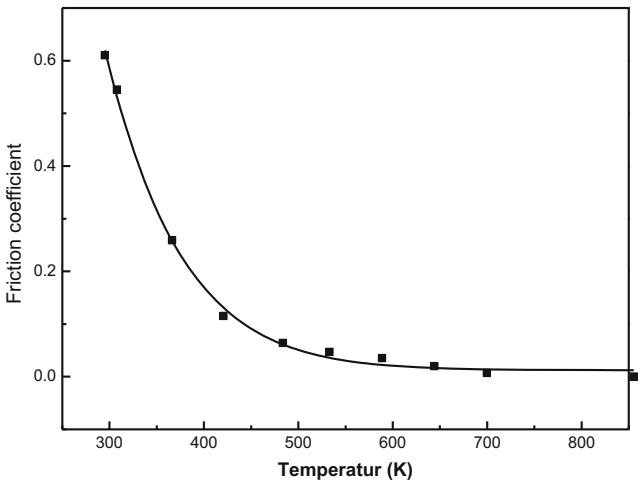

Fig. 5 Plot of friction coefficient as a function of temperature

The relative velocity of the contact interface between the tool and the workpiece at elemental area can be given as follows:

$$V_a = (1-\delta)(\omega_2 r + U\sin\theta) \tag{12}$$

where ω_2 is the rotating speed of the assisted shoulder, r is the length between the elemental area and the tool axis ($R_{\text{in}} \le r \le R_{\text{out}}$), θ is the angle between the welding direction and the r radius vector direction, and δ is the dimensionless slip rate which is given as follows [28]:

$$\delta = \frac{\nu_m}{\nu_t} = 1-\frac{\dot{\gamma}}{\nu_t} \tag{13}$$

where ν_t is the position-dependent tool velocity at elemental area dA, ν_m is the material flow velocity at that area, and $\dot{\gamma}$ is the slip rate which can be defined as follows:

$$\dot{\gamma} = \nu_t - \nu_m \tag{14}$$

Furthermore, assuming that the welding speed does not influence the slip rate for sliding or the deformation rate for sticking, then the dimensionless slip rate δ can be defined as follows:

$$\delta = \frac{\omega_m}{\omega_t} \tag{15}$$

where ω_t is the rotating speed of the tool at the elemental area and ω_m represents the rotating speed of the plastic material at that area.

The dimensionless slip rate δ lies in the range of 0 to 1. For sticking without slip $\delta=1$, that means all the plastic material at the interface are sticking to the tool and rotating with the tool as the tool rotating speed. For sliding without workpiece deformation $\delta=0$, that means no plastic material is sticking to the tool. The condition $0<\delta<1$ means that there are partial sticking or sliding at the tool-workpiece contact interfaces.

The heat generation rate due to friction for the assisted shoulder can be written as follows:

$$dp_{fa} = \mathrm{V}_a df = (1-\delta)(\omega_2 r + U\sin\theta)\mu_f P_2 dA \tag{16}$$

When the plastic material sticks to the tool, deformation heat is generated at the tool-workpiece contact interface. The conversion efficiency of deformational work into heat is η, and the contact shear stress τ_c is given by [16]:

$$\tau_{\text{c}} = \frac{\sigma_{\text{yield}}}{\sqrt{3}} \tag{17}$$

The heat generated due to plastic deformation at the elemental area dA may be calculated as:

$$dp_{sa} = \eta\delta(\omega_2 r + U\sin\theta)\tau_c dA \tag{18}$$

Since there are heat generated due to friction and plastic deformation at the tool-workpiece contact interface, then the total heat generation rate for the assisted shoulder would be approximately given as follows:

$$dp_a = dp_{fa} + dp_{sa} = \left[\eta\delta\tau_c + (1-\delta)\mu_f P_2\right](\omega_2 r + U\sin\theta)dA \tag{19}$$

Thus, the heat flux at the elemental area for the assisted shoulder would be given as follows:

$$q_a' = \frac{dp_a}{dA} = \left[\eta\delta\tau_c + (1-\delta)\mu_f P_2\right](\omega_2 r + U\sin\theta) \tag{20}$$

The total heat generated at the tool-workpiece contact interface can be partitioned between the workpiece and the tool based on their thermophysical properties. The ratio of the heat transported into the workpiece is f [29]:

$$f = \frac{J_W}{J_W + J_T} = \frac{\left(k\rho C_p\right)_W^{1/2}}{\left(k\rho C_p\right)_W^{1/2} + \left(k\rho C_p\right)_T^{1/2}} \tag{21}$$

where J_W is the total heat conducted to the workpiece and J_T is the total heat conducted to the tool.

The heat flux into the workpiece under the assisted shoulder can be approximately:

$$q_a = f\left[\eta\delta\tau_c + (1-\delta)\mu_f P_2\right](\omega_2 r + U\sin\theta) \tag{22}$$

2.2.2 Heat flux boundary of the tool pin with subsize concave shoulder

Due to reverse rotation direction, the relative velocity of the contact interface between the subsize concave shoulder and the workpiece at elemental area is expressed as:

$$V_s = (1-\delta)(\omega_1 r - U\sin\theta) \tag{23}$$

Similarly, the heat flux into the workpiece under the subsize concave shoulder can be approximately [26]:

Table 2 Specific heat capacity and thermal conductivity of 2024 Al alloy

Temperature (K)	298	373	473	573	673
$Cp/(J\cdot kg^{-1}\cdot K^{-1})$	921	921	1,047	1,130	1,172
$k/(W\cdot m^{-1}\cdot K^{-1})$	121.8	134.4	151.2	172.2	176.4

$$q_s = f\left[\eta\delta\tau_c + (1-\delta)\mu_f P_1\right](\omega_1 r - U\sin\theta) \tag{24}$$

where P_1 is the plunge force of plunge force of tool pin with subsize concave shoulder, ω_1 is the rotating speed of tool pin with subsize concave shoulder, and r is the length between the elemental area and the tool axis ($R_{po} \le r < R_{in}$).

The tool pin rotates with the subsize concave shoulder, so heat flux under the bottom of the tool pin is similar to that under the subsize concave shoulder. The heat flux boundary may be approximately expressed as [26]:

$$q_{pb} = f\left[\eta\delta\tau_c + (1-\delta)\mu_f P_1\right](\omega_1 r - U\sin\theta) \tag{25}$$

where r is the length between the elemental area and the tool axis ($0 \le r \le R_{pi}$).

In this study, a taper cylindrical tool pin is used and the thread on the pin is ignored. The heat flux for the side surface of the tool pin is given as [30]:

$$q_{ps} = f\left[\eta\delta\tau_c + (1-\delta)\mu_f \sigma_{\text{yield}}\right](\omega_1 r - U\sin\theta) \tag{26}$$

where σ_{yield} is the yield stress and r is the length between the elemental area and the tool axis ($R_{pi} < r < R_{po}$).

2.2.3 Velocity boundary conditions at the tool-workpiece contact interface

In this model, the translational welding speed of the tool is applied to the calculated domain as the inverse welding speed of the workpiec which is given as $-U$. The velocity of the surface in front of the tool is set as the welding velocity in reverse direction and the surface behind the tool is set as the outflow boundary. Under the tool-workpiece contact interfaces, the velocity condition is defined in terms of angular velocity of the tool to multiply the dimensionless slip rate.

2.2.4 Heat exchange boundary conditions of the surface of the workpiece

At the top surface of the workpiece beyond the shoulder, the boundary condition for heat exchange involves both convective and radiative heat transfer:

$$-k\frac{\partial T}{\partial n} = \sigma_e \varepsilon\left(T^4 - T_a^4\right) + \gamma(T - T_a) \tag{27}$$

where σ_e is the Stefan-Boltzmann constant (5.67×10^{-12}JK^{-4} cm^{-2} s^{-1}), ε is the external emissivity, γ is the heat transfer coefficient, and T_a is the ambient temperature.

At the bottom and side of the workpiece, due to intimate contact of the workpiece with the backing plate, the boundary condition for heat exchange involves only convective heat transfer:

$$-k\frac{\partial T}{\partial n} = \gamma(T - T_\infty) \tag{28}$$

At the other side of the workpiece, temperature is set at ambient temperature.

Table 3 The process parameters in RDR-FSW (the assisted shoulder is rotating in clockwise direction, while the pin is rotating in counter-clockwise direction in RDR-FSW)

Test no.	RDR-FSW		
	Welding speed (U, mm/min)	Rotating speed of assisted shoulder (ω_1, rpm)	Rotating speed of pin (ω_2, rpm)
1	100	−800	600
2	100	−800	800
3	100	−800	1,000
4	100	−800	1,200
5	50	−800	800
6	150	−800	800
7	200	−800	800
8	100	−600	800
9	100	−1,000	800
10	100	−1,200	800

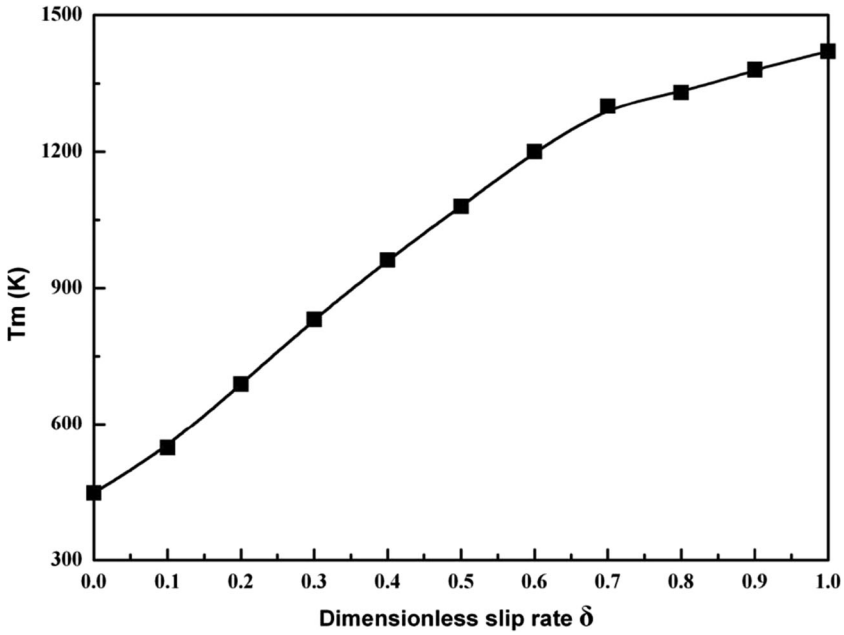

Fig. 6 Calculated peak temperature as a function of dimensionless slip rate (test no. 2)

In simulation of conventional FSW, heat flux boundary condition at the tool-workpiece contact interface at the tool pin are the same as to RDR-FSW, and the heat flux at the shoulder in conventional FSW are the same to that at the subsize concave shoulder in RDR-FSW except that the range of r is different. The other heat exchange boundary condition and the velocity boundary conditions are the same in conventional FSW and RDR-FSW except that the inverse velocity direction at the assisted shoulder in RDR-FSW simulation.

3 Solution method

Computations of the governing equations and their boundary conditions are performed employing the finite volume method discussed by Patankar [31]. This method is based on the cell-centered, nonstaggered grid method. The calculations of the coupled temperature field and velocity field are performed according to the semi-implicit method for pressure linked equations (SIMPLE) scheme. The process in the entire

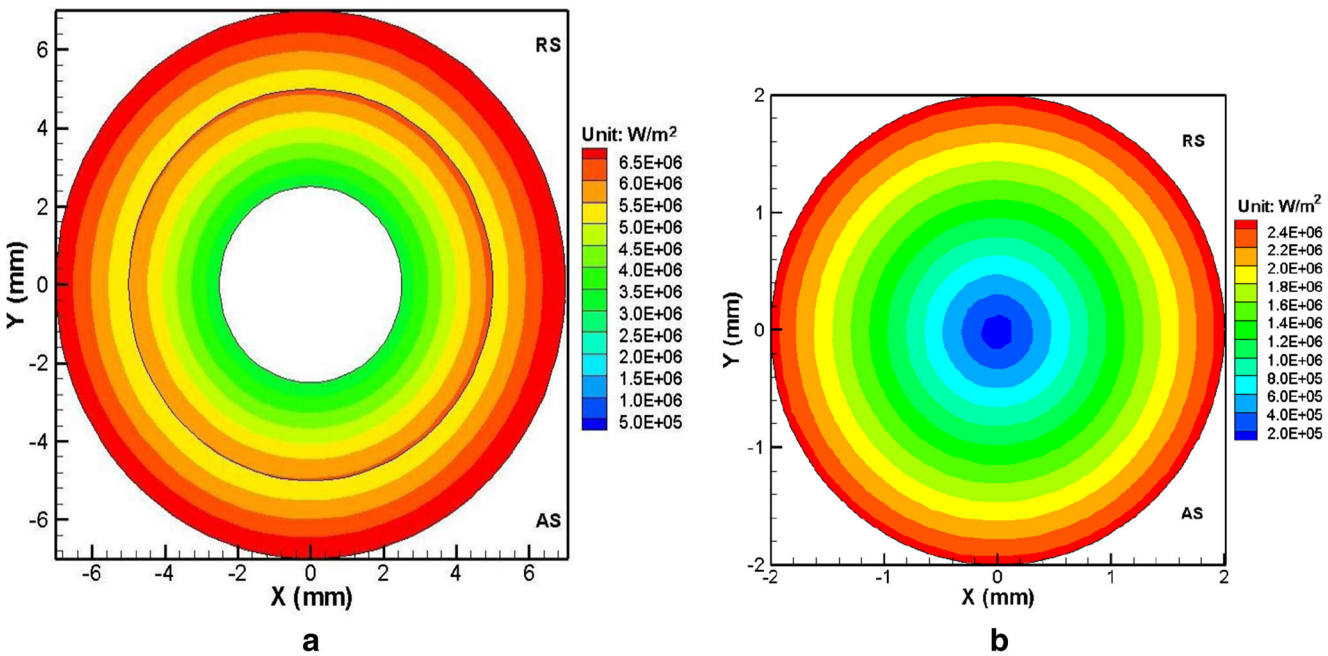

Fig. 7 Spatially distributed heat generation rate at the tool-workpiece contact interfaces for test No. 3 **a** at the shoulder (the *black line in the middle* shows the boundary of the subsize concave shoulder) and **b** at the bottom of the tool pin

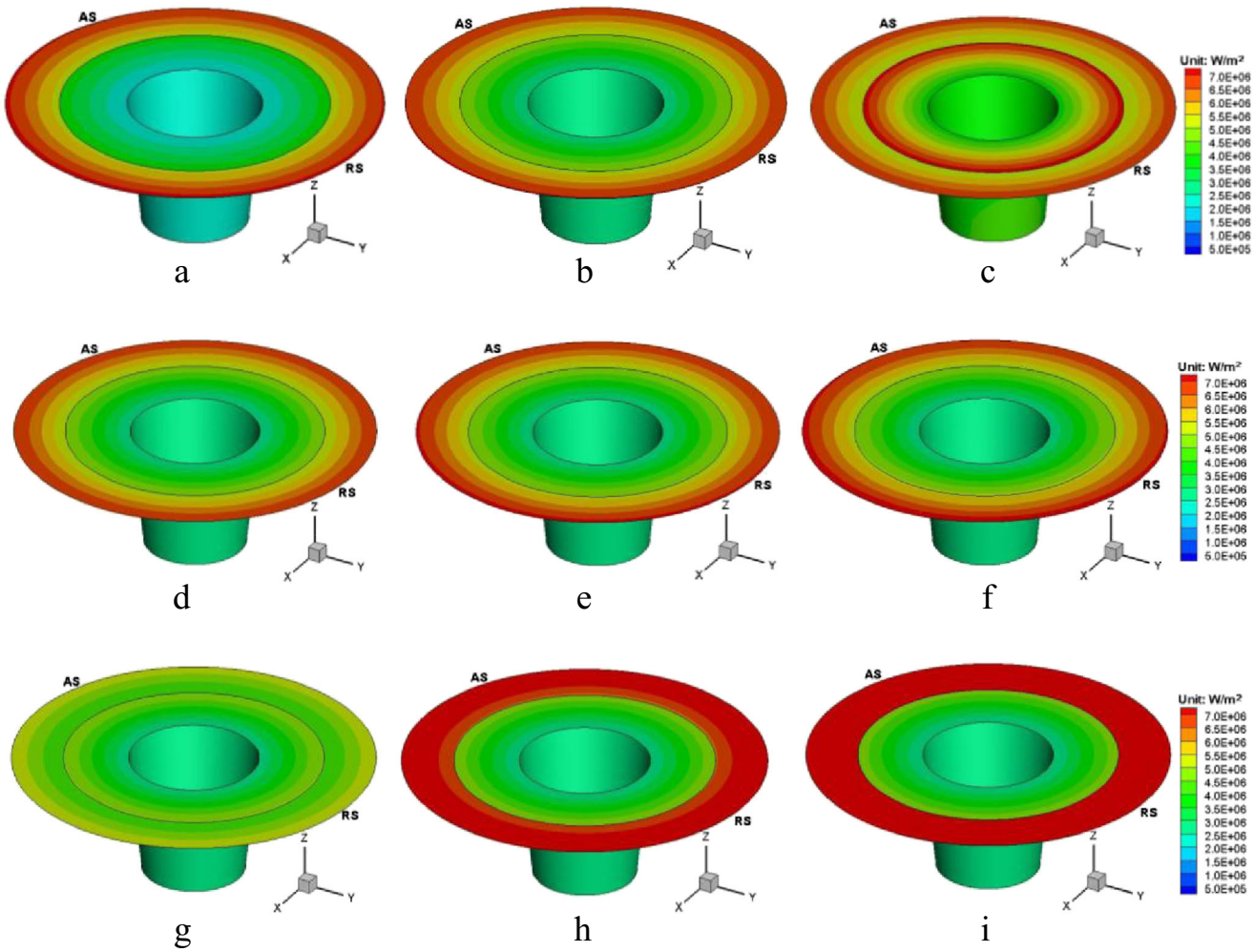

Fig. 8 Spatially distribution heat flux at the tool-workpiece contact interface under different welding conditions—**a** test no. 1, **b** test no. 2. **c** test no. 4, **d** test no. 5, **e** test no. 6, **f** test no. 7, **g** test no. 8, **h** test no. 9, **i** test no. 10

workpiece is modeled as single-phase non-Newtonian flow with appropriate source terms in the conservation equations. In order to test and assess grid independence of the solution scheme, many numerical experiments were performed. These experiments showed that a nonuniform grid mesh of 100 mm×100 mm×5 mm is adequate to describe the heat generation, material flow, and temperature field characteristics accurately. Finer grids are chosen to describe the portion of the domain which encompasses severe material flow and heat generation near the tool in order to resolve the plasticized material flow and heat convection. The computation is performed until the convergence criteria are reached.

4 Results and discussion

In this study, the workpiece material in this simulation is 2024 Al alloys. The variation of specific heat capacity and thermal conductivity of 2024 Al alloys with temperature is given in Table 2 [19]. The process parameters used in the simulation of RDR-FSW process are listed in Table 3. Axial pressure of assisted shoulder and the tool pin is chosen as 29.5 MPa.

4.1 Heat generation rates

The proportion of the heat generation at the tool-workpiece surface is determined by the tool geometry and the welding parameters. Figure 6 shows the calculated peak temperature as a function of dimensionless slip rate in test no. 2. It demonstrates that the slip/stick condition between the tool-workpiece has a significant influence on the peak temperature. Plastic deformation heat is the primary heat generation at the tool-workpiece contact interface. In this study, 0.25 was chosen as the value of the standard dimensionless slip rate (δ) in the following simulation because under such a value, the calculated peak temperature is about 800 K which is about 90 % of the melting point, and the calculated temperature matches well with the measured ones. In addition, when δ=0.25, the results

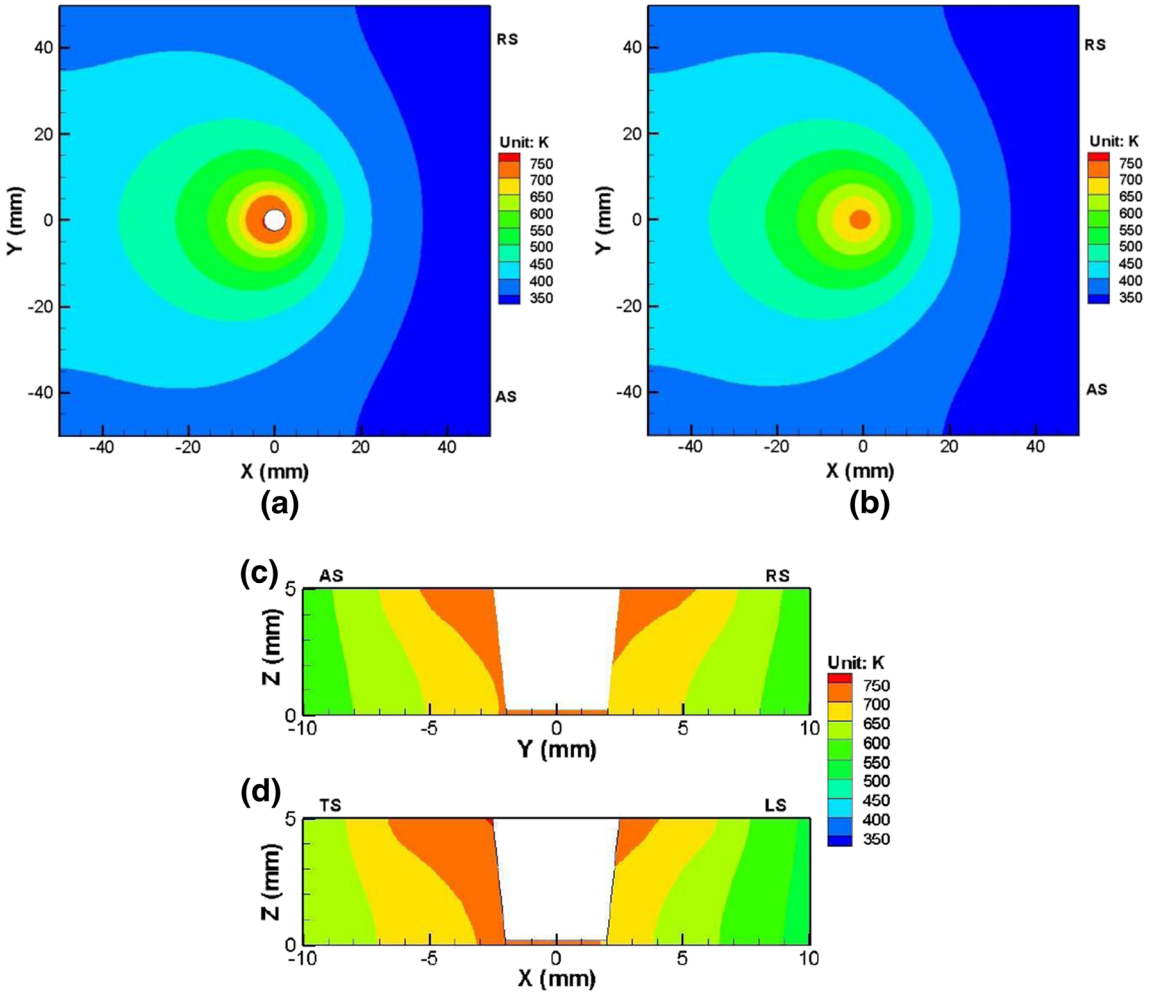

Fig. 9 Calculated temperature field for test no. 2. **a** Plane Z=5 mm, **b** plane Z=0 mm, **c** transverse section, **d** longitudinal section

are in good agreement with those in literature related to conventional FSW [28, 32].

The spatially distributed heat generation rate at the tool-workpiece contact interface for test no. 3 are showed in Fig. 7. Figure 7a shows that the heat generation pattern at the tool shoulder contact interfaces is nearly symmetrical on the tool axis. Most of the heat is generated at locations further away from the tool axis owing to a higher relative velocity between the workpiece and the shoulder. However, compared to the heat generation rate at the points with the same diameter, the heat generation rate ahead of the tool axis is slightly higher than that behind the tool axis. Because the temperature is relatively higher behind the tool, it leads to relatively smaller friction coefficient and flow stress there. The heat generation rate between the contact interfaces are within the order of 10^5–10^6 W/m^2. The maximum heat generation rate during the process is located at the outer diameter of the assisted shoulder where the relative velocity is highest. The heat generation rate at the bottom of the tool pin shows a similar feature to that of the shoulder but of lower value (Fig. 7b), because the radius of the tool pin is smaller and the relative velocity between the contact interface is lower. Nandan et al. reported similar trends in their research on conventional FSW [16].

Figure 8 depicts the spatially distributed heat flux at the tool-workpiece contact interfaces under different welding conditions. With the increase of the rotating speed of the tool pin with the subsize concave shoulder, the heat flux under the tool pin with subsize concave shoulder is increased, whereas the heat flux under the assisted shoulder is slightly decreased, as shown in Fig. 8a–c. Similarly, with increase of the rotating speed of the assisted shoulder, the heat flux under the assisted shoulder is increased, whereas heat flux under the tool pin with subsize concave shoulder is slightly decreased, as shown in Fig. 8g–i. The welding speed has little influence on the heat flux at the tool-workpiece contact interface as shown in Fig. 8d–f.

4.2 Calculated temperature fields

Figure 9 shows the calculated temperature fields in the RDR-FSW. The temperature profiles are compressed at the front of the tool but expanded behind it. The computed

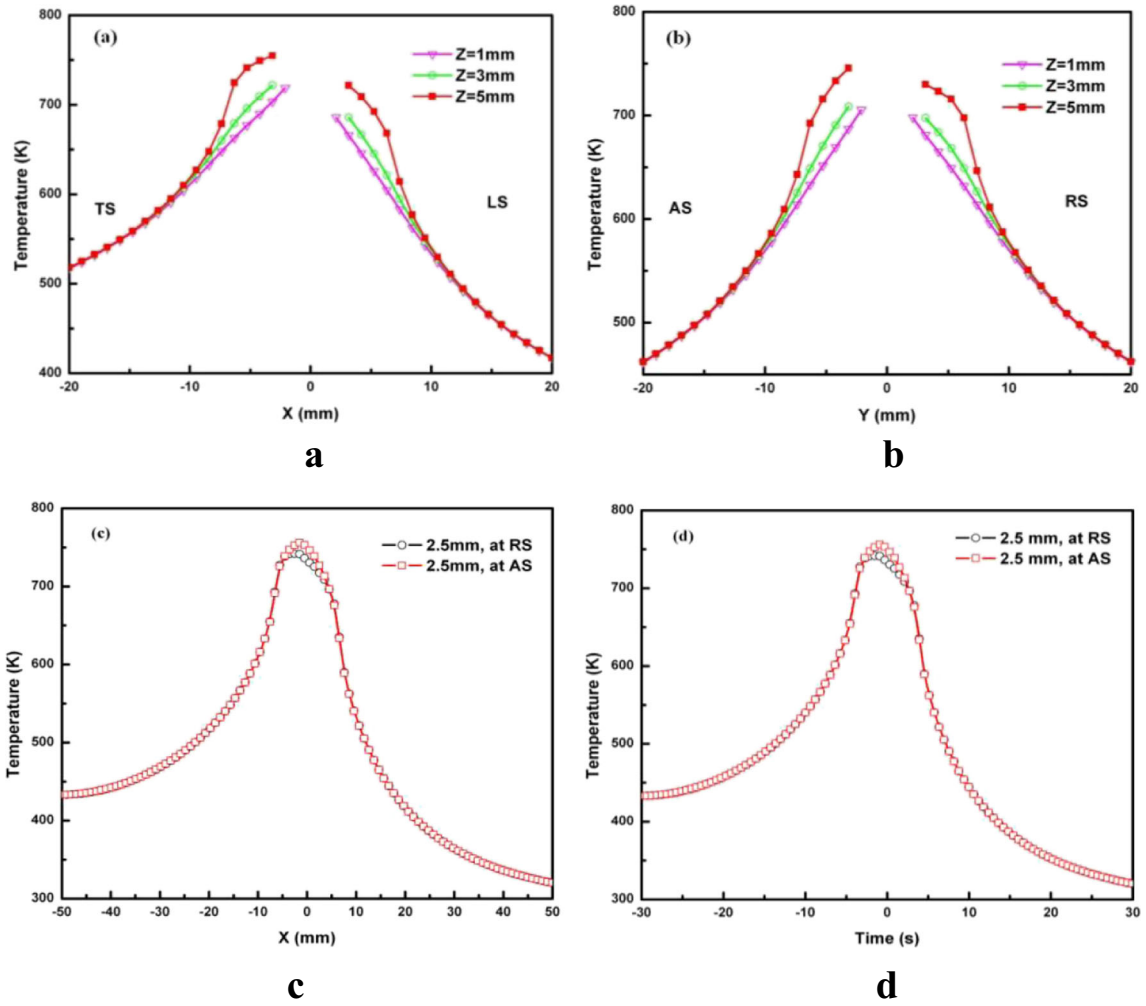

Fig. 10 Calculated temperature profile for test no. 2 **a** along the welding line at depths Z=1, 3, and 5 mm; **b** perpendicular to the welding line at depths Z=1, 3, and 5 mm; **c** along the welding line at the top of the workpiece, 2.5 mm from the centerline at AS and RS; and **d** temperature history at two points (top surface of workpiece, 2.5 mm from the centerline at AS and RS)

results are consistent with the fact that heat is supplied rapidly to the cold region of the workpiece ahead of the tool, while heat is transported at a slower rate to the material already preheated behind the tool due to the low diffusivity of the preheated material and the lower temperature gradient.

Figure 9a demonstrates that asymmetric temperature distribution exists near the tool pin at the top of the workpiece. There are relatively higher velocity and higher shearing rate at AS. The preheated plastic material is transported to AS under the motion of the assisted shoulder. Thus, in the vicinity of the tool, the temperature at AS is higher than that at RS. However, approximately symmetric temperature distribution is observed at the bottom of the workpiece (Fig. 9b). Since the tool pin and the assisted shoulder are separated and they rotate reversely, there are two opposing material flows near the tool so that the difference of heat generation rate between the AS and RS owing to the different relative velocity is weakened. Figure 9c, d depicts that at locations far away from the tool, the temperature profiles are almost identical at the AS and RS.

Temperature variation as a function of distance or time is shown in Fig. 10. Figure 10a demonstrates the predicted temperature distribution along the weld line (varied X coordinates) and at different depth (varied Z coordinates). It is seen that temperatures behind the tool are about 20–30 K higher than that ahead of the tool, because of the moving of the tool along the welding direction. Figure 10b demonstrates the predicted temperature distribution along the y axis (perpendicular to the weld line) and at different depth (varied Z coordinates). It shows that in the vicinity of the tool, the temperature values at the AS are about 5–20 K higher than that at the RS, and the temperature difference between AS and RS decreases as the depth increasing. Figure 10c shows the predicted temperature distribution at Y=2.5 mm along the weld line at the top surface of the workpiece. Thermal histories would be constructed from

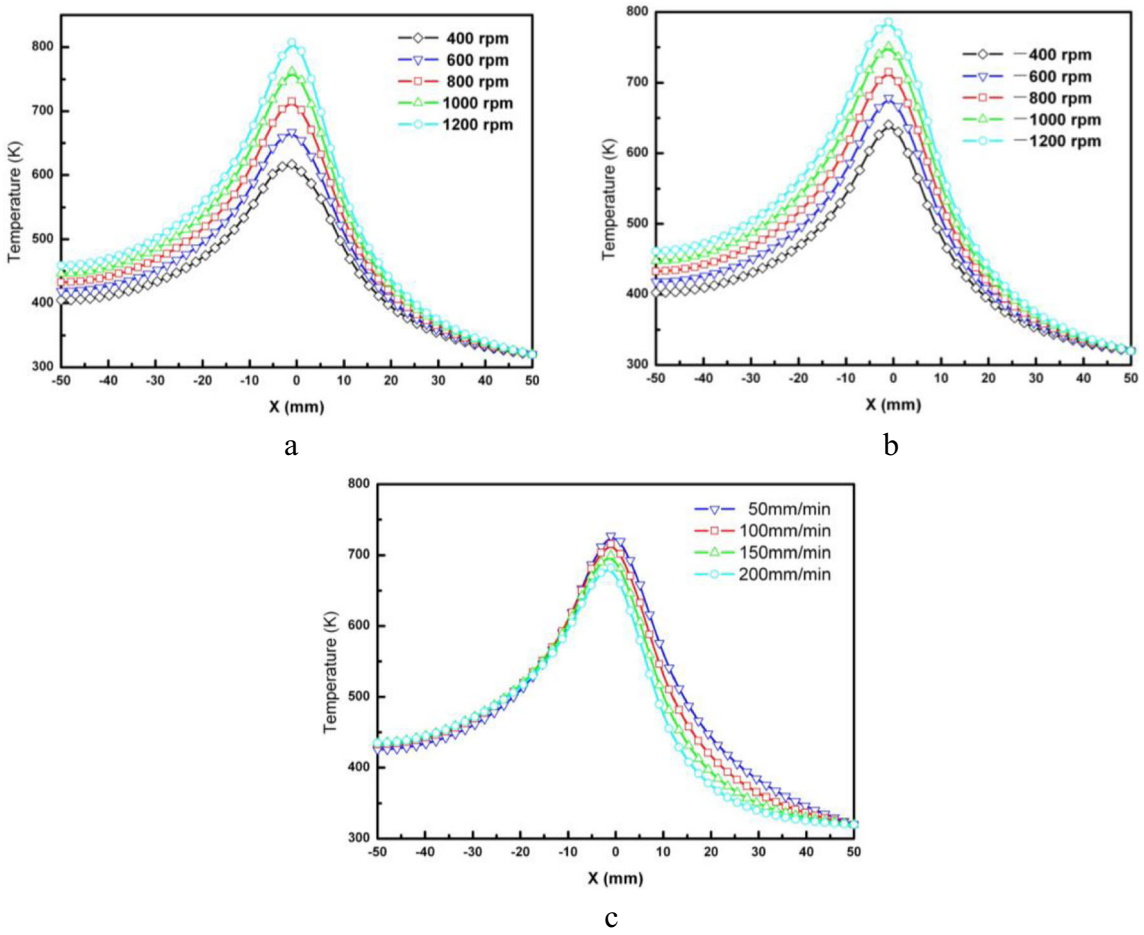

Fig. 11 Calculated temperature profile along a line (Y=−2.5 mm, Z=3 mm) at AS under different welding conditions—**a** different rotating speed of the tool pin with subsize concave shoulder, where ω_2=−800 rpm, U=100 mm/min; **b** different rotating speed of the assisted shoulder, where ω_1=800 rpm, U=100 mm/min; **c** different welding speed, where ω_1=800 rpm, ω_2=−800 rpm

the steady-state temperature distribution by replacing the distance traveled by the tool with the time [16]. Figure 10d depicts the temperature-time curves for two points locating at 2.5 mm away from the weld line on the top surface at AS and RS, respectively. It illustrates that there is a rapid temperature-rising stage when the tool approaches to the monitoring locations, while there is a comparatively slower cooling stage as the tool moves away from it. Near the tool, the temperature at AS is slightly higher than that at RS. With the distance increasing away from the tool, there is a little temperature difference between AS and RS.

Figure 11 shows the calculated temperature profiles along a line with 2.5 mm away from the weld centerline at plane Z=3 mm at AS. As the rotating speed of the tool pin with subsize concave shoulder or the assisted shoulder increases (as is shown in Fig. 11a, b), the peak temperature increases and the high temperature region (over 600 K) is enlarged. When the welding speed increases, the peak temperature decreases slightly as shown in Fig. 11c.

Figure 12 illustrates that the measured and calculated temperature-time profile at different monitoring locations are in good agreement. The model can be used to predict the temperature profiles and cooling rates in RDR-FSW process.

4.3 Material flow

Figure 13 shows the calculated material flow velocity near the tool. It can be seen from Fig. 13a that the maximum velocity during RDR-FSW is about 0.14 m/s, which is about 25 % of the maximum tool velocity at the diameter outside of the assisted shoulder. Although the assisted shoulder enlarges the diameter of the total shoulder, it has little effect on material flow velocity under the subsize concave shoulder and near the tool pin due to its reverse rotating direction. The velocity around the tool pin is confined to a relatively small region which leads to a relatively smaller isoviscosity region in the RDR-FSW compared to conventional FSW. Figure 13b shows that the peak velocity

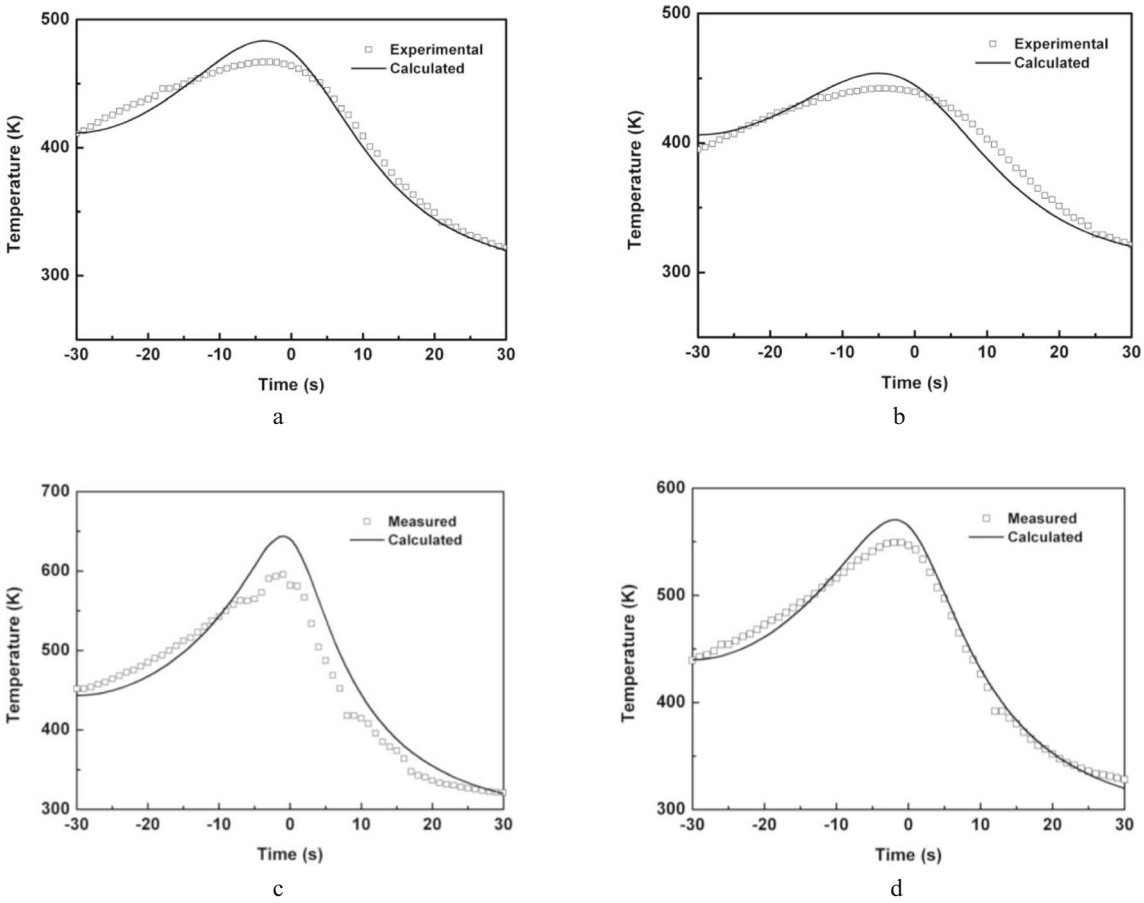

Fig. 12 Comparison between measured and calculated temperature-time profile at Z=3 mm plane **a** 20 mm away from the centerline at RS for test no. 1, **b** 24 mm away from the centerline at RS for test no. 1, **c** 8 mm away from the centerline at RS for test no. 3, and **d** 12 mm away from the centerline at RS for test no. 3

locates at the periphery of the assisted shoulder where the effects of the shoulder are fairly pronounced. However, due to high viscosity, the momentum decays rapidly away from the tool, the effects of the tool do not reach far away, and it results in rapidly reducing of velocity away from the tool. Material flow region near the tool at RS is slightly larger than that at AS, as shown in Fig. 14.

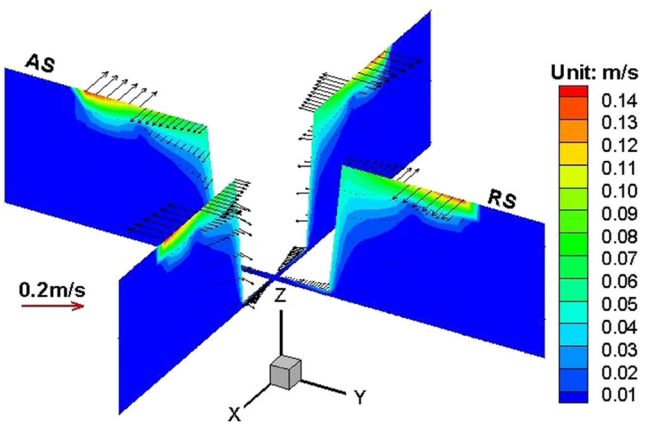

Fig. 13 Calculated material flow velocity near the tool for test no. 2

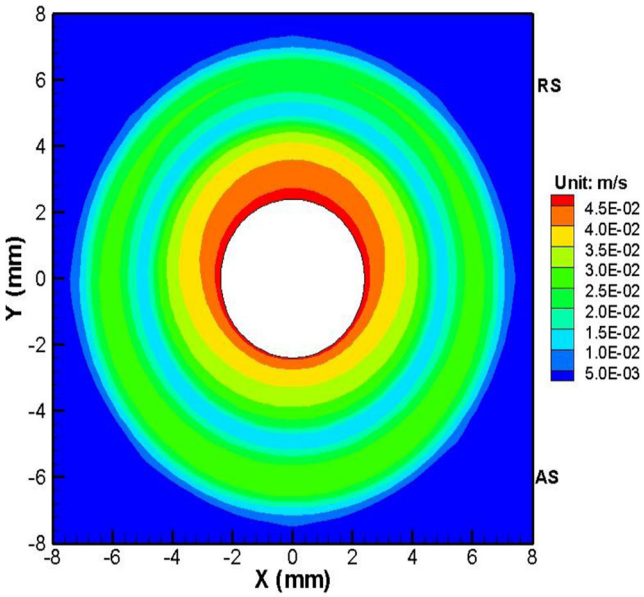

Fig. 14 Calculated velocity near the tool for test no. 2 at horizontal plane Z=4 mm

Table 4 The process parameters in RDR-FSW and conventional FSW (the assisted shoulder is rotating in clockwise direction, while the pin is rotating in counter-clockwise direction in RDR-FSW; tool rotating is in counter-clockwise direction in conventional FSW)

Test no.	RDR-FSW			Conventional FSW	
	Welding speed (U, mm/min)	Rotating speed of assisted shoulder ω_1 (rpm)	Rotating speed of pin (ω_2, rpm)	Welding speed (U, mm/min)	Rotating speed (ω, rpm)
C1	100	−600	600	100	600
C2	100	−800	800	100	800
C3	100	−1,000	1,000	100	1,000

4.4 Comparison of RDR-FSW and conventional FSW

In this part, the heat generation, temperature distribution, and isoviscosity region in RDR-FSW are compared with those in conventional FSW at the same parameters (Table 4).

Figure 15 shows a typical comparison of the temperature field at different horizontal plane in RDR-FSW and conventional FSW for test no. C1. As shown in Fig. 15a, the temperature is slightly higher on the AS than the RS both in RDR-FSW process and conventional FSW, and this is in agreement

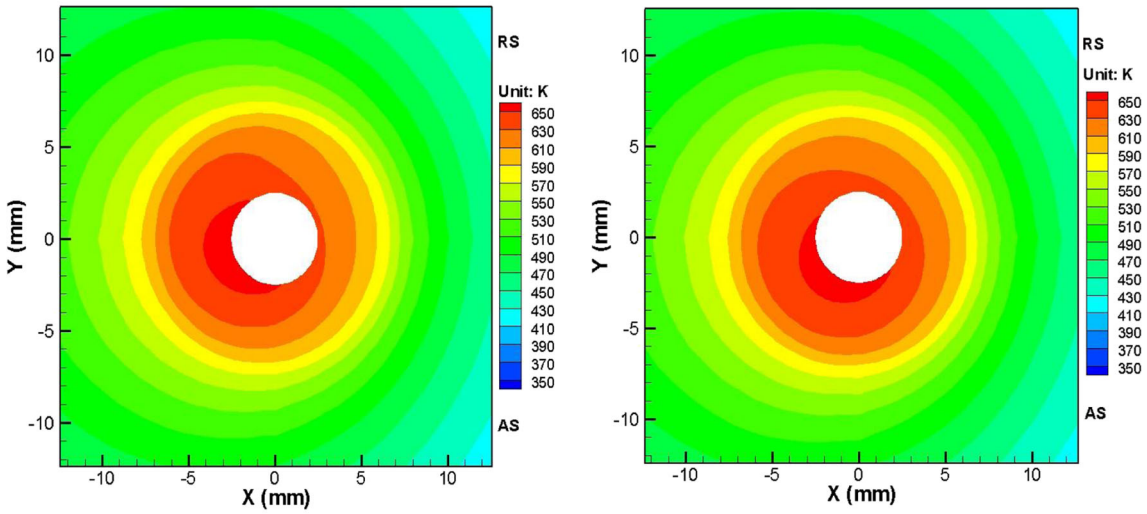

a at plane Z=5mm, left for RDR-FSW, right for FSW

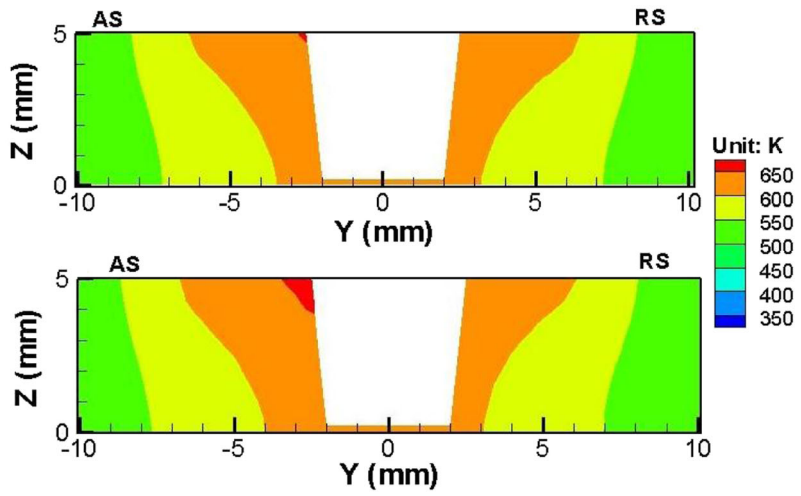

b at transverse section, top for RDR-FSW, bottom for conventional FSW

Fig. 15 Comparison of temperature field in RDR-FSW and conventional FSW (units in K) for test no. C1 **a** at plane Z=5 mm (*left* for RDR-FSW, *right* for FSW) and **b** at transverse section (*top* for RDR-FSW, *bottom* for conventional FSW)

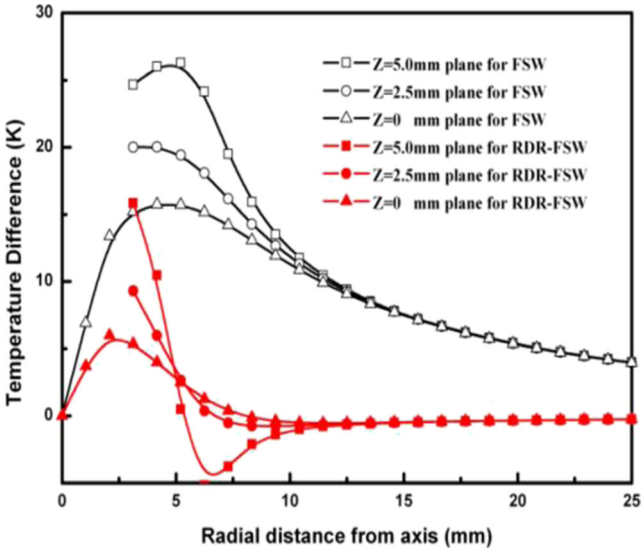

Fig. 16 Temperature difference between AS and RS in RDR-FSW and conventional FSW at different depth along transverse section for test no. C2

with previous research results in literature [16, 26]. However, during the RDR-FSW, the symmetry of the temperature field is improved. That means the reversely rotating assisted shoulder has alleviated the temperature asymmetry. Figure 15b compares the temperature field at the transverse section. It could be found that the high temperature region (over 600 K) at RS in RDR-FSW process is larger than that in conventional FSW. However, at AS, that region in RDR-FSW process is smaller than that in conventional FSW. This also proves that the temperature asymmetry during RDR-FSW process has been alleviated.

Figure 16 shows the temperature difference between AS and RS in RDR-FSW and conventional FSW at different depth along transverse section. The temperature differences will first increase as the radial distance is increased from the tool axis and reach the peak near the edge of the tool. Then, it will reduce as the radial distance increasing. It is obviously shown that the temperature difference between AS and RS in RDR-FSW is lower than that in conventional FSW. That means the symmetrical characteristic of the temperature field has been improved during the RDR-FSW process. Since the assisted shoulder and tool pin are separated and rotating reversely, the difference of the heat generation rate between the AS and RS owing to the difference of relative velocity has been decreased; also, there are plastic material flows of reverse direction.

The isoviscosity near the tool could be useful to predict the geometry of thermal mechanical affected zone (TMAZ). Reports show that the critical viscosity for aluminum alloy was in the range of 10^6 to 10^7 kg·m^{-1}·s^{-1}, above which no significant plastic flow occurs [16, 26]. Figure 17 depicts the calculated isoviscosity region near the tool. It could be found that the isoviscosity region of 2.5×10^6 kg/(m·s) in RDR-FSW is smaller than that in the conventional FSW. The isoviscosity has been confined to a relatively small region owing to reverse rotation of the assisted shoulder.

5 Conclusions

1. A three-dimensional model is developed to conduct the numerical simulation of the heat generation and temperature distribution in RDR-FSW process. Both the friction and the plastic deformation are considered to determine the heat generation rate, and appropriate value of the dimensionless slip rate is obtained.
2. Due to the assisted shoulder and tool pin being separated and rotating reversely, the difference of heat generation rate between the AS and RS owing to the difference of relative velocity is weakened. The two reverse flow is beneficial to the uniform distribution of temperature at AS and RS, and enhancement of the plastic material flow around the tool.
3. The numerical simulation results of heat generation, material flow, and temperature profiles show that the RDR-FSW process is of great application potential in industry. Through adjusting the rotating speed of the tool pin and assisted shoulder independently, the heat input and the temperature field can be optimized to achieve high quality of welds.

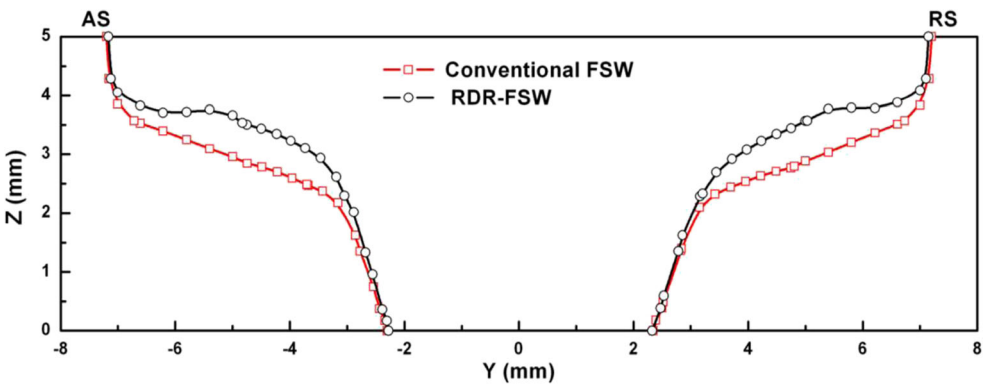

Fig. 17 The calculated isoviscosity line (2.5×10^6 kg·m^{-1}·s^{-1}) in RDR-FSW and conventional FSW at transverse section for test no. C3

Acknowledgments The authors are grateful to the State Key Laboratory of Advanced Welding and Joining at Harbin Institute of Technology in China (Grant No. AWJ-Z13-02) and the Sino-German Center for the Promotion of Science (Grant No. GZ-739) for the financial support to this research.

References

1. Mishra RS, Ma ZY (2005) Friction stir welding and processing. Mater Sci Eng R 50(1):1–78
2. Nandan R, Debroy T, Bhadeshia HKDH (2008) Recent advances in friction-stir welding-process, weldment structure and properties. Prog Mater Sci 53(6):980–1023
3. DebRoy T, Bhadeshia H (2010) Friction stir welding of dissimilar alloys—a perspective. Sci Technol Weld Join 15(4):266–270
4. Vilaça P, Thomas W (2012) Friction stir welding technology. Adv Struct Mater 8:85–124
5. Chen C, Kovacevic R (2004) Thermomechanical modeling and force analysis of friction stir welding by the finite element method. J Mech Eng Sci 218(5):509–519
6. Zimmer S, Langlois L, Laye J, Bigot R (2010) Experimental investigation of the influence of the FSW plunge processing parameters on the maximum generated force and torque. Int J Adv Manuf Technol 47(1–4):201–215
7. Li JQ, Liu HJ (2013) Effects of welding speed on microstructures and mechanical properties of AA2219-T6 welded by the reverse dual-rotation friction stir welding. Int J Adv Manuf Technol 68(9–12): 2071–2083
8. Thomas WM, Norris IM, Staines DG, Watts ER (2005) Friction stir welding—process developments and variant techniques. The SME Summit 2005, Oconomowoc
9. Li JQ, Liu HJ (2013) Characteristics of the reverse dual-rotation friction stir welding conducted on 2219-T6 aluminum alloy. Mater Des 45:148–154
10. Gök K, Aydin M (2013) Investigations of friction stir welding process using finite element method. Int J Adv Manuf Technol 68(1–4): 775–780
11. Zhang Z, Zhang HW (2007) Material behaviors and mechanical features in friction stir welding process. Int J Adv Manuf Technol 35(1–2):86–100
12. Nandan R, Roy GG, Lienert TJ, DebRoy T (2006) Numerical modelling of 3D plastic flow and heat transfer during friction stir welding of stainless steel. Sci Technol Weld Join 11(5):526–537
13. Prasanna P, Rao BS, Rao GKM (2010) Finite element modeling for maximum temperature in friction stir welding and its validation. Int J Adv Manuf Technol 51(9–12):925–933
14. Colegrove PA, Shercliff HR, Zettler R (2007) Model for predicting heat generation and temperature in friction stir welding from the material properties. Sci Technol Weld Join 12(4):284–297
15. Neto DM, Neto P (2013) Numerical modeling of friction stir welding process: a literature review. Int J Adv Manuf Technol 65(1-4):115–126
16. Nandan R, Roy GG, DebRoy T (2006) Numerical simulation of three-dimensional heat transfer and plastic flow during friction stir welding. Metall Mater Trans A 37(4):1247–1259
17. Zhang Z, Zhang HW (2014) Solid mechanics-based Eulerian model of friction stir welding. Int J Adv Manuf Technol. doi:10.1007/s00170-014-5789-4
18. Arora A, De A, DebRoy T (2011) Toward optimum friction stir welding tool shoulder diameter. Scr Mater 64(1):9–12
19. Wu CS, Zhang WB, Shi L, Chen MA (2012) Visualization and simulation of the plastic material flow in friction stir welding of aluminium alloy 2024 plates. Trans Nonferrous Metals Soc China 22(6):1445–1451
20. Al-Badour F, Merah N, Shuaib A, Bazoune A (2014) Thermo-mechanical finite element model of friction stir welding of dissimilar alloys. Int J Adv Manuf Technol. doi:10.1007/s00170-014-5680-3
21. Nandan R, Roy GG, Lienert TJ, DebRoy T (2007) Three-dimensional heat and material flow during friction stir welding of mild steel. Acta Mater 55(3):883–895
22. Perzyna P, Wojno W (1966) On the constitutive equations of elastic/viscoplastic materials at finite strain. Arch Appl Mech 18:85
23. Seidel TU, Reynolds AP (2001) Visualization of the material flow in AA2195 friction-stir welds using a marker insert technique. Metall Mater Trans A 32(11):2879–2884
24. Sheppard T, Wright DS (1979) Determination of flow stress: part 1 constitutive equation for aluminum alloys at elevated temperatures. Metals Technol 6(1):215–223
25. Sheppard T, Jackson A (1997) Constitutive equations for use in prediction of flow stress during extrusion of aluminum alloys. Mater Sci Technol 13(3):203–209
26. Cho HH, Hong ST, Roh JH, Choi HS, Kang SH, Steel RJ, Han HN (2013) Three-dimensional numerical and experimental investigation on friction stir welding processes of ferritic stainless steel. Acta Mater 61(7):2649–2661
27. Awang M, Mucino VH, Feng Z, David SA (2005) Thermo-mechanical modeling of friction stir spot welding (FSSW) process: use of an explicit adaptive meshing scheme, Proceedings of the SAE 2005 World Congress & Exhibition, 2005 April 11–14
28. Schmidt H, Hattel J (2005) Modelling heat flow around tool probe in friction stir welding. Sci Technol Weld Join 10(2):176–186
29. Lienert TJ, Stellwag JWL, Grimmett BB, Warke RW (2003) Friction stir welding studies on mild steel. Weld J 82(1):1s–9s
30. Mehta M, Chatterjee K, De A (2013) Monitoring torque and traverse force in friction stir welding from input electrical signatures of driving motors. Sci Technol Weld Join 18(3):191–197
31. Patankar SV (1980) Numerical heat transfer and fluid flow. Hemisphere, Washington
32. Schmidt H, Dickerson TL, Hattel J (2006) Material flow in butt friction stir welds in AA2024-T3. Acta Mater 54(4):1199–1209